

pubs.acs.org/JPCC Article

High Mobility HgTe Quantum Dot Films with Small Energy and Dynamic Disorder

Haozhi Zhang, John C. Peterson, Augustin Caillas, and Philippe Guyot-Sionnest*



Cite This: J. Phys. Chem. C 2024, 128, 6726-6734



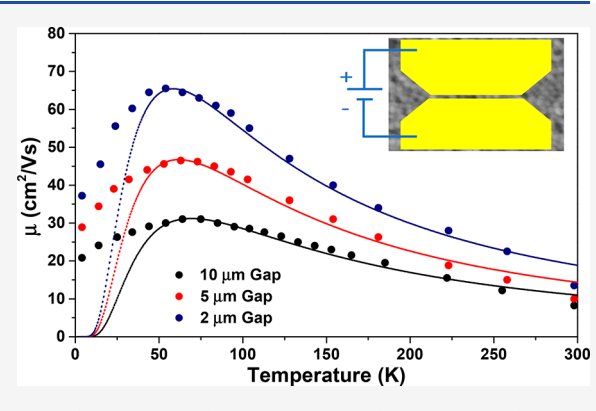
ACCESS

III Metrics & More

Article Recommendations

s Supporting Information

ABSTRACT: The transport properties of HgTe colloidal quantum dot films are studied from 4 to 300 K with larger and more monodispersed quantum dots than previously. With nanocrystals of 14 nm diameter and 6.5% size distribution, a peak mobility of 65 cm²/(V s) is measured at 65 K for state-resolved transport in the 1Se state. Above 70 K, the mobility is band-like, but it follows the Marcus electron hopping model, while being far below the Mott−Ioffe−Regel limit. At 65 K, the average hopping time is as fast as 1 ps and getting close to the estimated dephasing time, or dynamic disorder, of the 1Se state, suggesting that coherence may exist for some neighboring dots. At lower temperatures, the mobility decreases for low bias, but it is temperature-independent for high bias due to field-driven transport. The Efros−Shklovskii variable range hopping model gives localization lengths of ∼100 nm, also suggesting large coherent



domains. Twice lower mobility and shorter localization lengths are obtained with a 10 μ m channel compared to a 2 μ m channel, suggesting a possible percolation of the more conducting domains.

I. INTRODUCTION

Colloidal quantum dots (CQD) have potential in optoelectronics, including photodetection, light-emitting diodes, and field effect transistors, through the tunability of their optical and electronic properties, and some performances benefit from high carrier mobility. Mobilities around 10-30 cm²/(V s), similar to those of good organic semiconductors, have been obtained in CQD films by ligand exchange, surface passivation, small size dispersion, annealing, necking, and doping control.²⁻⁵ A recent report of 300 cm²/(V s) for PbSe CQD superlattices⁶ exceeds other reports by an order of magnitude. For high mobility CQDs films, an increasing mobility upon cooling is called band-like.²⁻⁴ With doped CQDs, such a bandlike trend down to 0 K would be evidence of metallic conductivity. Metallic conductivity in metal nanoparticle solids has been observed, irrespective of being disordered or ordered,9 and this can be explained by the many conductive channels available between metallic nanoparticles. 10 Similarly, metallic transport can be achieved with highly doped quantum dots, 11 and the metal-insulator transition has been reported using highly doped, necked, and disordered ZnO nanocrystal solids 12-14 as well as with highly doped necked superlattices of PbS CQD.¹⁵

In the limit of low doping, with transport occurring through specific quantum dot states, metallic conductivity and bandlike mobility down to 0 K have not been observed. Using HgTe CQDs and a polar solution exchange to reduce interparticle distance, Lan et al. reported the first CQD system that showed state-resolved and high electron mobility, with a

peak mobility of 8 cm²/(V s) at 80 K and band-like down to that temperature. ¹⁶ These CQDs had a size distribution of \sim 10%, and the band-like transport could be explained by thermally activated electron hopping between dots, limited by static energetic disorder. At lower temperature, the mobility dropped to less than 0.1 cm²/(V s) at 4 K, but the delocalization length, extracted from a variable range hopping model, provided possible evidence of delocalization of electrons across 2–3 dots at low temperature.

HgTe quantum dots are a good system for further transport studies. They benefit from low degeneracy $1S_{\rm e}$ and $1P_{\rm e}$ conduction band states, which allow to identify state-resolved transport upon charging, and the doping of a small number of electrons can be controlled. HgTe CQDs are also studied for infrared optoelectronic devices which motivates achieving even high carrier mobility.

This work extends the prior study of Lan et al. ¹⁶ to slightly larger and more monodisperse HgTe CQDs, aiming to increase the mobility by reducing static energy disorder. In addition, dynamic disorder could play a role. Dynamic disorder has been discussed in the context of crystalline organic films²⁰

Received: December 8, 2023
Revised: April 1, 2024
Accepted: April 3, 2024
Published: April 15, 2024





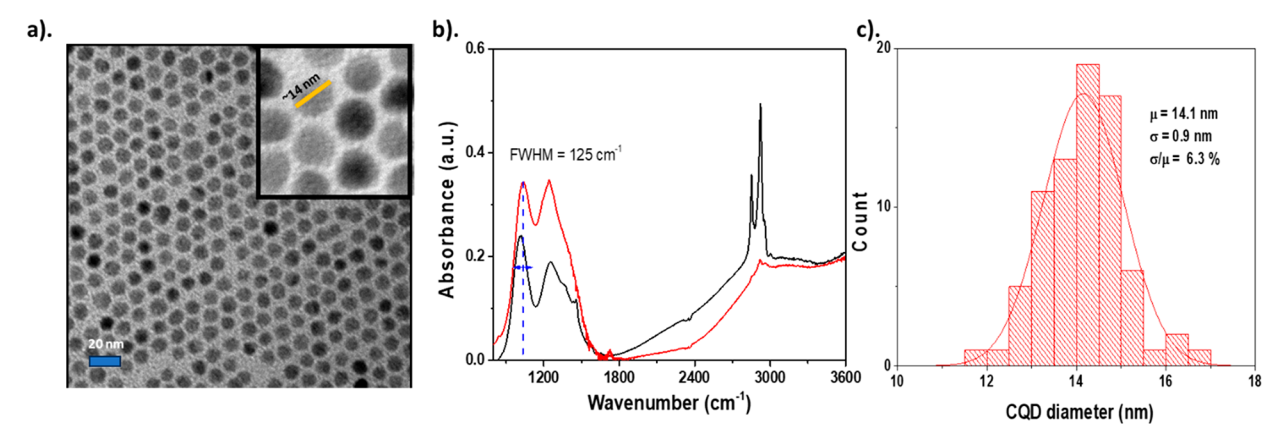


Figure 1. (a). TEM image of synthesized CQDs, with magnification ×49K and in inset ×120K. (b) Absorption spectrum at 300 K of the CQDs film before (black) and after (red) hybrid ligand exchange. (c) Distribution of TEM sizes in (a), with a mean size of 14.1 nm and a dispersion of 6.3%.

in order to explain their band-like behavior and their lower mobility than bulk semiconductors, but to our knowledge, not yet with CQD films. In CQD films, the dynamic disorder is unlikely to be from the overall motion of the heavy nanoparticles but rather from the rapid fluctuations of the energies of the quantum dots due to elastic collision with internal phonons. In this context, the more monodisperse and larger HgTe CQDs are rather unique since they display a narrow $1S_{\rm e}{-1P_{\rm e1/2}}$ line width 21,22 and possibly small dynamic disorder. This work reports a detailed transport study of this system, including the effects of channel length and electric field at low temperatures.

II. METHODS

Materials. $HgCl_2$ (≥98%), $HgBr_2$ (97%), 1,2-ethanedithiol (≥98.0% (GC)), HCl (ACS reagent, 37%), 2-mercaptoethanol (≥99.0%), butylamine (99.5%), isopropyl alcohol (≥99.7%, FG), and anhydrous solvents (octane, toluene, chlorobenzene, and methanol) were purchased from Sigma-Aldrich and used as received. Anhydrous N_iN -dimethylformamide (DMF, 99.8%) and $HgCl_2$ (98+%) were purchased from Alfa Aesar and used as received. Oleylamine was degassed at 100 °C for several hours. Bis(trimethylsilyl)telluride (98%) was purchased from Acros and stored inside the freezer in a nitrogen glovebox. N-type Si wafers (residue ≤0.005 ohm·cm) with 300 nm thick thermal oxide were purchased from WaferPro.

HgTe Synthesis. The synthesis of HgTe CQDs is modified from a previously reported method. A solution of 36 mg of HgCl₂ (0.133 mmol), 21 mg of Hg(OAc)₂ (0.067 mmol), and 4 mL of oleylamine (OAm) is heated to a 90 °C temperature inside a nitrogen glovebox until all Hg compounds have dissolved. The solution is then rapidly heated to the desired temperature for nanocrystal growth (110 °C, with larger nanocrystals obtained at higher temperature). Meanwhile, 10 μ L of bis(trimethylsilyl)telluride (TMS₂Te, 0.035 mmol) is dissolved in 500 μ L of anhydrous toluene, and 65 μ L of 1 M TOPTe is dissolved in 500 μ L of oleylamine. The toluene must be fully transparent after adding the TMS₂Te to ensure that no small nuclei of Te are formed. The TMS₂Te solution is rapidly injected into the Hg compound solution and heated at the injection temperature for exactly 1 min. After the 1 min reaction of TMS₂Te, the TOPTe solution is injected dropwise and slowly over 5 min. The solution is then quenched with 4 mL of cold anhydrous toluene.

The QDs are precipitated with isopropanol, centrifuged, redispersed in toluene, and precipitated once more. The resulting QDs are dispersed in octane. For transfer to DMF, the octane solution is mixed with 5 mL of DMF containing 0.025 mM HgCl₂, 140 μ L of 2-mercaptoethanol, and 400 μ L of butylamine in a glovebox. Shaking transferred the HgTe QDs to the DMF phase. The DMF solution is cleaned twice with octane. The solution is then precipitated with antisolvent toluene and centrifuged at 4000 rpm for 1 min; the final precipitate is redispersed in a small amount of DMSO.

Device Fabrication. The FET substrate is a doped Si wafer with 300 nm of thermally grown SiO₂. The FET is made with three pairs of evaporated gold electrodes with width/gap length of 10 μ m/500 μ m, 5 μ m/250 μ m, and 2 μ m/100 μ m. The gap lengths are verified by SEM to have less than 0.1 μ m variation as shown in Figure S1. The substrate is heated to 70 °C and treated with 2% HCl/H2O as this helps the wetting of the CQD polar solution. The hybrid ligand exchange HgTe CQD is drop-casted onto the FET in air at 70 °C and quickly dried by removing excess solution from an edge with KimWipes. After the drop-casted HgTe film is dried on the hot plate for 1 h under nitrogen, a layer of 10% weight fraction of polyvinyl butyral dissolved in chlorobenzene is spin-coated on the surface of the FET. The device is further dried under nitrogen overnight at room temperature. The device is then used for measurement.

Mobility Measurement. The differential mobility of the HgTe film is measured using the slope of the FET transport curves. The formula is $\mu = \frac{\partial I_{\rm sd}}{V_{\rm gate}} \frac{L}{WC_i}$, where $I_{\rm sd}$ is the source—drain current, $V_{\rm g}$ is the gate potential, $V_{\rm sd}$ is the source—drain bias voltage, C_i is the calculated capacitance of the 300 nm SiO₂ gate dielectric, L is the channel length, and W is the channel width. The samples are contacted with spring plunge contacts, held between a copper base and a copper back plate, and screwed together for strong thermal contact. They are in a high vacuum inside a closed-cycle cryostat that can reach 4 K with a cold shield. The sample temperature is taken from a silicon diode on the copper base.

Transmission Electron Microscopy (TEM). TEM images were obtained on a FEI Technai Spirit or F30 microscope at 300 kV.

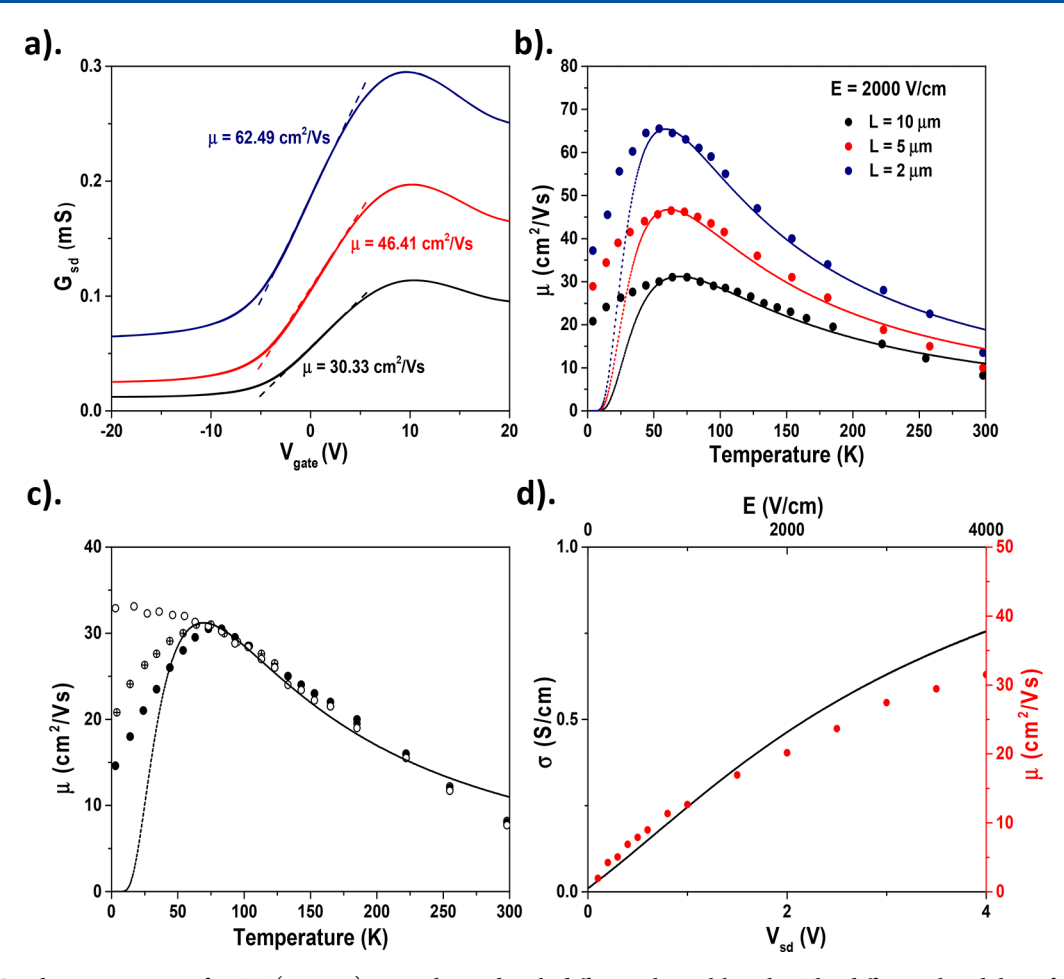


Figure 2. (a) Conductance curves of FETs (at 70 K) were obtained with different channel lengths. The differential mobility of 1Se electrons is shown as the dashed lines. Black: $10~\mu m$; red: $5~\mu m$; blue: $2~\mu m$. (b). Differential mobility measured from 4 to 298 K, with different channel lengths. The solid dots are differential mobility measured from the conductance curve on the FET, and dashed lines are the Marcus model (see Table 1). (c) Mobility of the electrons at $10~\mu m$ channel length, 298 K, and different bias voltages. Solid: 1~V; cross: 2~V; open: 4~V. Measured conductance (black line) and differential mobility (red dot) were measured with different bias voltages at 4~K and $10~\mu m$ channel length.

Size Distribution Measurement. CQD sizes are analyzed manually from the TEM images, and the size histogram is fitted with a Gaussian function.

III. RESULTS AND DISCUSSION

Synthesis of HgTe CQDs with Improved Size Dispersion. The synthesis of nonaggregated HgTe CQDs follows Shen et al.²³ It used the injection of TMS₂Te into a solution of HgCl₂ in oleylamine. The size dispersion of these CQDs was about 10% or greater, and solid state ligand exchange with short thiols gave mobility on the order of 10⁻² cm²/(V s). Using polar phase exchange with a "hybrid" ligand protocol, with halide ions and short organic thiols and amines, Lan et al. improved the mobility by more than 2 orders of magnitude up to 8 cm²/(V s). Here, we used a modified synthetic protocol to obtain a narrower size distribution. 22,24 The synthesis is done in a two-step injection of first TMS₂Te followed by TOPTe into a solution containing a mixture of Hg(OAc)₂: HgCl₂ dissolved in oleylamine. Hg(OAc)₂ is chosen as a more reactive Hg precursor that is easily soluble. The ratio of Hg(OAc)₂ to HgCl₂ is kept just below the ratio that leads to an unstable colloidal solution during the nucleation phase. A TEM of the resulting sample is shown in Figure 1a. The sample is naturally n-doped leading to a strong intraband absorption with the narrow 1S_e-1P_{e1/2} spinorbit transition²² at low energy, as shown in Figure 1b. The size dispersion is \sim 6.3% around the mean 14 nm diameter, based on the TEM image, as shown in Figure 1c.

After the synthesis, the solution is cleaned once and transferred to a polar solution of DMF, following Lan and co-workers. 16,17 The precipitate of HgTe is redispersed in DMSO with 10 $\mu \rm L$ of 2-mercaptoethanol. After a second size-selective precipitation with added toluene, the precipitate is redissolved in neat DMSO and drop-casted on the field effect transistor (FET) substrate at 70 °C, which prevents aggregation during solvent evaporation. All of the processing is done in ambient conditions. A polymer layer (~300 nm) of polyvinyl butyral (PVB) is cast by spin-coating on the dot film and dried under nitrogen overnight to encapsulate the film and ensure a stable doping during the measurements.

Electrical Transport. In order to explore possible effects of delocalization, FET substrates are made with channel lengths of 10, 5, and 2 μ m. The widths of the FET channels are respectively set to 500, 250, and 100 μ m for a constant length-to-width ratio. This ensures that the conductances of the HgTe films are identical across the three devices if the carrier mobilities are the same. All measurements are reported for films with a doping of about 0.5 electrons/dot in the 1Se state, which corresponds to the highest differential mobility, as shown in Figure 2a. For all other figures, the differential

mobility reported is taken around 0 V gate bias, and the conductivity measurements are taken at zero gate bias, thus ensuring a fixed uniform doping across the samples.

The highest $1S_e$ mobility previously reported for 15 nm HgTe films with hybrid ligand exchange was $18 \text{ cm}^2/(\text{V s})$. While our study shows similar state-resolved features, the HgTe dots films studied here differ slightly in having a rather spherical shape, and the films are subjected to 70 °C overnight annealing. Figure 2a shows that the highest mobility, measured directly from the FET, is $\sim 30 \text{ cm}^2/(\text{V s})$ for a channel length of $10 \ \mu \text{m}$ and reaches $65 \text{ cm}^2/(\text{V s})$ for a channel length of $2 \ \mu \text{m}$.

We note that on all samples the smaller channel lengths led to a higher mobility. Prior work did not report such effect of the channel length on the mobility, but it also did not explore such narrow channels. SEM imaging is used to confirm the channel length for all electrodes, and the deviation is less than 50 nm. The SEM images of the films resolve the individual quantum dots (Figure S1). The packing is disordered with a few empty gaps/cracks in the film of the size of a few dots but without larger defects. Figure 2b shows the FET mobility from 4 to 298 K across devices of the three channel lengths. The mobility shows band-like transport down to 70 K, decreasing at lower temperature, but it is so strongly affected by the applied bias that it does not necessarily trend to zero at 0 K as shown in Figure 2b and Figure 2c.

Transport above 70 K. Above 70 K, transport is ohmic in the bias range. The Marcus hopping model of electrons between quantum dots is taken as 16,26,27

$$\mu(T) = \frac{2\pi}{6} \frac{e(d+l)^2}{\hbar} \frac{J^2}{\sqrt{4\pi\lambda(k_{\rm B}T)^3}} \exp\left(\frac{-(\lambda+\Delta G)}{4\lambda k_{\rm B}T}\right) \tag{1}$$

where d is the dot diameter of 14.1 nm and l is the spacing between the dots surfaces taken to be 0.5 nm. The fitted parameters are J, the electronic transfer integral or coupling energy, and ΔG , which is an energy barrier that reflects the stated energy disorder. The reorganization energy is estimated as 16,27

$$\lambda = \frac{e^2}{4\pi\varepsilon_0} \left(\frac{1}{r} - \frac{1}{2(r+l)} \right) \left(\frac{1}{\varepsilon} - \frac{1}{\varepsilon_{\rm st}} \right) \tag{2}$$

where r is the dot radius, $\varepsilon_{\rm st}$ is the static dielectric constant, and ε is the optical dielectric constant in the infrared region. We estimate $\varepsilon_{\rm st}$ for the film of CQDs to be in the same proportion as for bulk HgTe where the static dielectric constant is $\varepsilon_{\rm st}=21$ and the optical dielectric constant is $\varepsilon=15.6$. Therefore, taking the high-frequency optical index of the polar exchanged CQDs films as 2.7, this gives $\varepsilon=7.6$ and $\varepsilon_{\rm st}=9.8$. With the same values of r and l as those above, the estimated reorganization energy is $\lambda=4.2$ meV. Figure 2b shows the best fit of the Marcus model above 70 K. The fitted coupling energy J and energy disorder ΔG are given in Table 1. The values are within 20% of the values reported by Lan et al. ¹⁶ The slightly larger dot size, the slightly larger coupling, and the slightly smaller disorder energy collectively contribute to the higher mobility.

The higher mobility obtained with the small gap length gives a larger J and a smaller ΔG . Given that the same drop-cast film covers the three devices on the same FET, such a variation cannot be easily explained, but it may reflect some coherent domain size effect, as discussed further below.

Table 1. Fitting Parameters for the Marcus Model and Mobility Measurements

gap le (μπ	ngth n)	mobility at 70 K $(cm^2/(V s))$	J (meV)	$\frac{\lambda}{(\text{meV})}$	$\frac{\Delta G}{(\mathrm{meV})}$
10)	30.3	2.1	4.2	7.9
5	5	46.4	2.2	4.2	7.3
2	2	62.5	2.5	4.2	7.0

When the hopping time is faster than the dephasing time of the states, the hopping picture should be switched to a coherent process. A similar situation exists for metals, which is when the mean free path is just as long as the interatomic distance. This is the Mott–Ioffe–Regel (MIR) criterion, In the absence of thermal disorder, an estimate of the MIR mobility is given as $\mu_{\rm MIR} \approx \frac{e(d+l)^2}{\hbar}$. Phis gives a $\mu_{\rm MIR}$ of 3000 cm²/(V s) for the HgTe CQD film, which is a much larger mobility than the measured value, supporting the use of the incoherent Marcus electron transfer model to explain the band-like behavior.

Another measure of macroscopic metallic behavior in 2D films is when the square conductance becomes greater than the quantum conductance $2e^2/h \sim 0.077$ mS, which was shown to be possible with highly doped PbS quantum dot monolayer superlattice, even with mobility less than $10 \text{ cm}^2/(\text{V s})^{15}$ Here, the square conductance of the film in Figure 2a at 0 V gate bias is about 20 times smaller than the quantum conductance, while the film is also about 10 layers thick, and this is consistent with hopping conductance. A similar criterium for metallic behavior is that the average conductance between nanocrystals is larger than the quantum conductance. 10 Taking the interdot conductance as σd where d is the interdot center-to-center distance, the interdot conductance in the films here is about 140 times smaller than the quantum conductance. Overall, the HgTe CQD system appears to be clearly in the hopping transport regime even though it displays band-like behavior down to 65 K and some of the highest mobility reported.

As discussed by Lan et al., 16 the validity of the hopping

As discussed by Lan et al., ¹⁶ the validity of the hopping picture becomes less clear when looking at the microscopic times scales. The mobility can be related to an average hopping time as $\tau_{\rm hop} = \frac{e(d+1)^2}{6\mu k_{\rm B}T}$. With the 65 cm²/(V s) mobility obtained here, $\tau_{\rm hop} \sim 1$ ps, at 65 K, which is 2–3 times shorter than in prior work. ¹⁶ 1 ps is also typical of electron–phonon thermalization times such that the picture of individual electrons hopping incoherently, from 1S_e to 1S_e across different dots and thermalizing at each hop, is strained. Moreover, the mobility is a macroscopic average while the films are disordered such that there must be faster hopping times

Another time scale introduced in this work is the $1S_e$ state dephasing, which is a measure of dynamic disorder. Delocalization should be possible only if the state dephasing is slower than the electron transfer time. The $1S_e$ state dephasing time is not directly measurable, but the HgTe CQDs system is unique in having a well-resolved $1S_e-1P_{e1/2}$ transition as shown in Figure 1b. Prior measurements gave a homogeneous full width at half-maximum $\Delta \tilde{\nu} \sim 70 \pm 15$ cm⁻¹ at 300 K. Assuming a linear narrowing with lower temperature, the width becomes 15 ± 3 cm⁻¹ at 65 K. This corresponds to a coherence time $T_2 = \frac{1}{\pi c \Delta \tilde{\nu}} = 0.7 \pm 0.15$ ps. The $1S_e$ state dephasing time could possibly be much shorter if

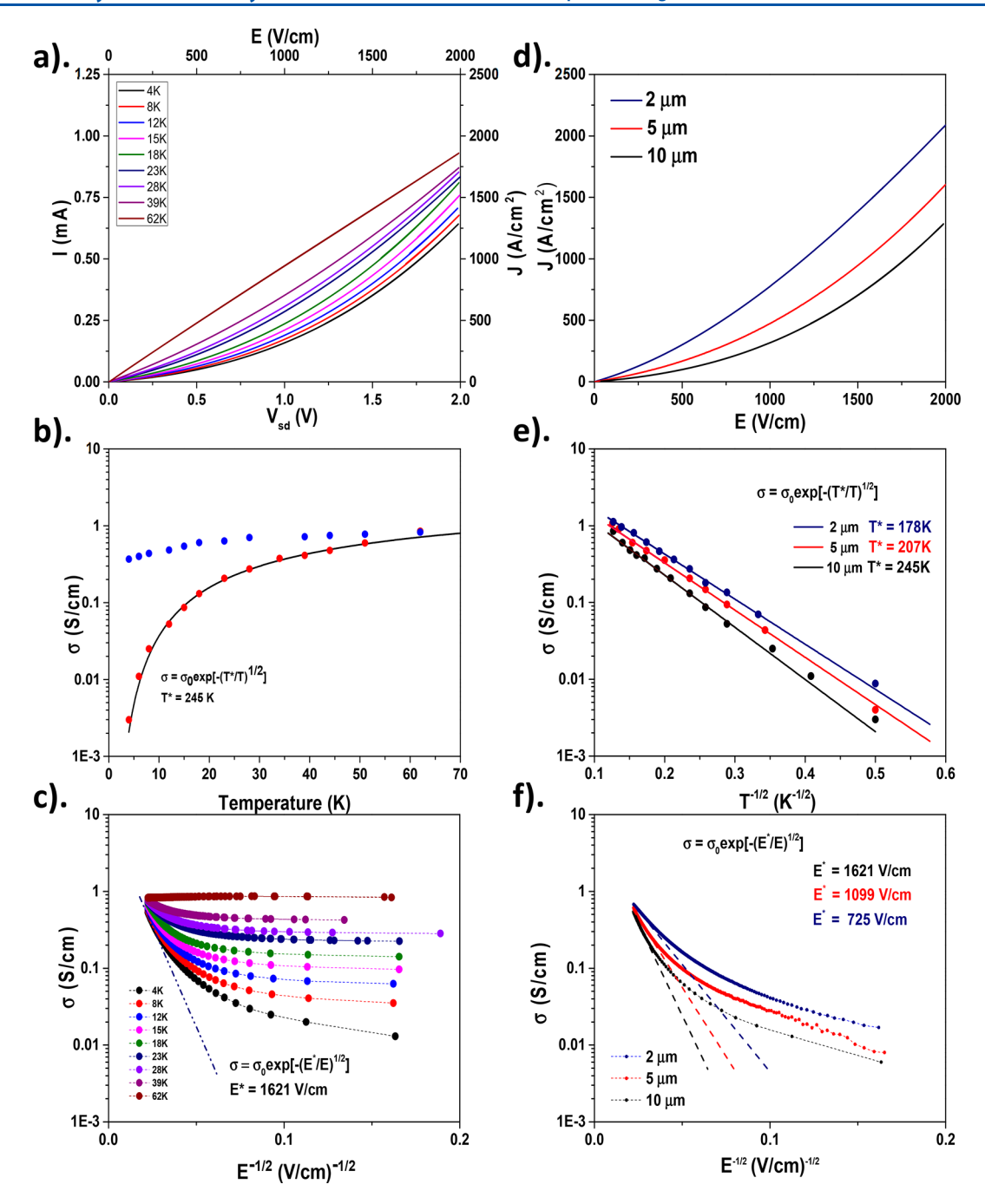


Figure 3. (a) I-V curve with T ranging from 4 to 62 K. (b) Conductivity of the CQD film versus temperature at different bias (red: 0.02 V; blue: 2 V). The black curve is the fitted data using the ES-VRH model. (c) Conductivity of HgTe CQDs plotted against the inverse root of the electric field, from 4 to 62 K. Current density versus electric field for HgTe CQD film measured at different channel lengths, with film thickness of 100 nm and T=4 K. Black: channel length = 10 μ m; red: 5 μ m; blue: 2 μ m. (e) Log of current density versus the inverse root of temperature, with a low electric field of 25 V/cm. Black: channel length = 10 μ m; red: 5 μ m; blue: 2 μ m. (f) Conductivity of HgTe CQDs at 4 K plotted against the inverse root of the electric field for different channel lengths. The dotted line corresponds to the asymptotic linear fit toward the high field.

dephasing is very correlated for $1\mathrm{S_e}$ and $1\mathrm{P_{e1/2}}$. However, it is also possible that the $1\mathrm{S_e}$ dephasing time is not much shorter than the dephasing of the transition, in which case it is similar to the average hoping time of 1 ps. In this case, coherence could be established over some number of well-coupled CQDs within the films, even though transport is not yet delocalized through the whole films.

Transport below 60 K. Figure 2c shows that the system starts to be non-ohmic below 60 K in the same bias range probed. Figure 2d shows the increasing conductance with

increasing bias for the device with a channel length of 10 μ m at 4 K. At 4 K, the mobility increases more than 100-fold with increasing bias, from 0.2 cm²/(V s) at $V_{\rm sd}$ = 0.1 V to 32 cm²/(V s) at $V_{\rm sd}$ = 4 V. In fact, at 4 V bias, the mobility does not drop at all as temperature decreases, and this does not fit an activated transport model. The qualitative explanation is that at such high bias per dot, transport becomes field-driven instead of thermally activated.

This low-temperature conductivity can be quantitatively discussed using the variable range hopping model. Figure 3a

shows the I-V curves of the device with 10 μ m channel length, with temperature ranging from 4 to 62 K. The I-V curve is strongly nonlinear at 4 K, but close to ohmic at 62 K, such that the mobility is strongly field dependent at 4 K, whereas this dependence vanishes above $\sim\!60$ K. Figure 3b shows the conductivity as a function of temperature for a fixed bias of 2 and 0.02 V, with the channel length of 10 μ m. It demonstrates a trend toward zero conductance at low bias as temperature decreases while the higher bias data show much smaller conductivity changes.

The Efros-Shklovskii theory of variable range hopping, ²⁸ ES-VRH, explains that at low temperatures and low field, electrons hop further than nearest neighbors, while the conductance is field-independent and temperature-dependent as

$$G \propto \exp(-\sqrt{T^*/T}) \tag{3}$$

On the other hand, at high field and low temperatures, when eV between dots becomes larger than $k_{\rm B}T$, the ES-VRH predicts a non-ohmic temperature-independent conductance given by

$$G \propto \exp(-\sqrt{E^*/E}) \tag{4}$$

where E is the applied field. In this regime, the electron transport between CQDs is purely field driven, and the hopping distance shortens with an increasing field. When E is much larger than E^* , electrons hop to the nearest neighbors, in which case the conductance tends to a constant, mimicking metallic transport. In the VRH model, both E^* and T^* depend on the "localization" length.

Experimentally, the T^* value is determined by low bias measurements. Because the current becomes very small at low field and low temperature, the FET derived differential mobility measurement becomes noisy. Therefore, we instead directly analyzed the conductivity from the I-V curves at zero gate bias. The low bias data in Figure 3b are fitted with eq 3, giving T^* around 245 K. The agreement with the fit worsens at the lowest temperatures, with the fit underestimating the current at 4 K by a factor of 2.3. In addition to the onset of field-driven effects, this deviation can be partly due to thermal drift of the closed-cycle cryostat at 4 K and by Joule heating. As discussed at the end, we used a COMSOL simulation to verify that, given the small bias and current, Joule heating is not responsible for the effects reported here.

The T^* predicted by the ES-VRH model is given as $T^* = \beta e^2/(4\pi \epsilon \epsilon_0 k_B \xi)$. Effectively, $k_B T^*$ scales as the Coulomb interaction over a distance equal to localization length ξ . β is a numerical constant of order unity, but there is a range of values proposed. It was determined to be $\beta = 2.8$ by Efros and Shklovskii for homogeneously doped semiconductors. Later work by Skinner et al. gave a value of $\beta = 8.1$ for semiconductor quantum dot films, and this is the value used here. For the dielectric constant, we used $\epsilon = 7.3$ estimated using the optical dielectric constant of HgTe CQD films. Using $T^* = 245$ K, the extracted localization length is ~75 nm, which is about 5 dot diameters. This value is very subject to the choice of β and ϵ , but it is large enough to suggest some degree of delocalization across the dots.

At high field and low temperatures, the transport trends to the ES-VRH prediction of $\sigma \propto \exp(-\sqrt{E^*/E})$. Figure 3c shows the log of the conductance versus the inverse root of the electric field and shows indeed a linear asymptotic limit at high

field. The asymptotic slope gave $E^*=1621\pm240$ V/cm. Yu et al. proposed that the variable range hopping conductance converges to the case of nearest-neighbor hopping when the external field is significantly larger than $E_0=2k_{\rm B}T/e\xi$. Using the estimate for ξ described before, we get $E_0>6000$ V/cm, which is larger than the maximum electric field applied in our experiments. Therefore, even at high field in this experiment, we are not yet reaching nearest-neighbor hopping. However, the convergence of conductance at high fields in Figure 3c suggests that we are approaching the constant conductance of nearest-neighbor hopping.

The ES-VRH model directly relates T^* and E^* by $E^* = k_B T^*/2e\xi$. This gives a second estimate of the electron localization length ξ , independent of the choice of β and ε , which is calculated to be 65 nm. This is in close agreement with the value in the previous section and confirms a rather long localization length of about 5 dots. Figure 3d shows the current density vs the electric field for the three gap lengths of 10, 5, and 2 μ m at 4 K. All channel lengths show a nonlinearity, while the higher mobility is obtained for the shorter channel. For the three channel lengths, Figure 3e shows the conductance as a function of temperature at a low electric field, which is used to obtain the T^* . Figure 3f shows the conductance as a function of the electric field at 4 K, which is used to obtain E^* from the asymptotic slope at high field.

The trend across the three channel lengths also allows one to rule out a contact Schottky barrier as a dominant source of the nonlinearity. Indeed, a contact resistance would scale inversely to the contact width, as $R_{\rm contact} \propto \frac{1}{W}$, while the film resistance scales as $R_{\rm Film} \propto \frac{L}{W}$. The current density would then scale as $J \propto \frac{E}{\frac{A}{W}+B}$ such that, if contacts are a dominant contribution, the current density decreases with reduced channel length and channel width, which is opposite to the data shown in Figure 2d.

The extracted values of E^* , T^* , and ξ for the different channel lengths are shown in Table 2. The ratio from the two

Table 2. Parameters Extracted from the Plots Using ES-VRH Theory^a

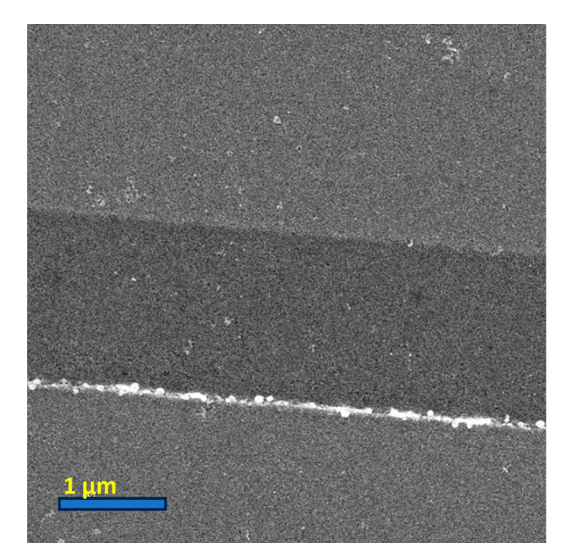
gap length $(\mu \mathrm{m})$	E* (V/cm)	T* (K)	$\xi (\beta e^2 / 4\pi \varepsilon \varepsilon_0 k_{\mathrm{B}} T^*) \ \mathrm{(nm)}$	$\xi (k_{\mathrm{B}}T^{*}/2eE^{*}) \ \mathrm{(nm)}$	ratio of ξ
10	1621 ± 241	245 ± 24	75	65	0.86
5	1099 ± 197	207 ± 20	90	81	0.90
2	725 ± 165	178 ± 18	104	106	1.01

[&]quot;Error bars are estimated at around 15% for E^* and about 10% of the value for T^* .

estimates of ξ is rather constant given the error bars for T^* and E^* , and there is a consistent increase in the localization length with decreasing channel length.

The localization length is an average property. The trend of a longer localization length with a narrower channel length may be interpreted as the system being close to a percolation threshold. This effect would arise from the inhomogeneous disorder in the films, as seen by the SEM images, and would be superimposed on the VRH model.

Possibly related effects were observed when applying a larger bias, up to the point of destroying the devices. Figure 4 shows the SEM images of devices after applying a high voltage (10 V)



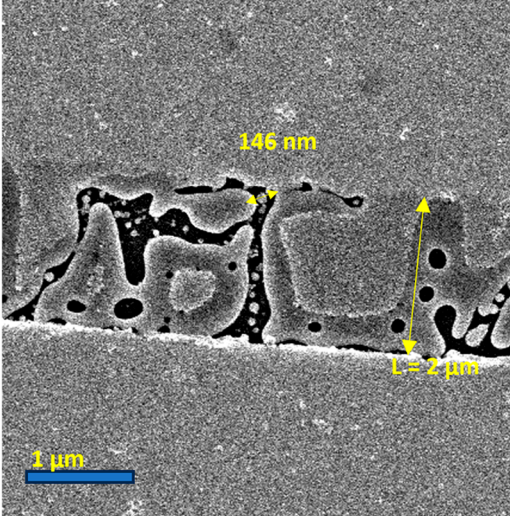


Figure 4. HgTe CQD films drop-casted between Au electrodes with a channel length of 2 μ m. Left: before a 10 V pulse is applied; Right: after the electric pulse, the conductive paths of the CQD films. One sees empty areas, surrounded by areas that appear molten, while other areas still have the graininess of the nanocrystals.

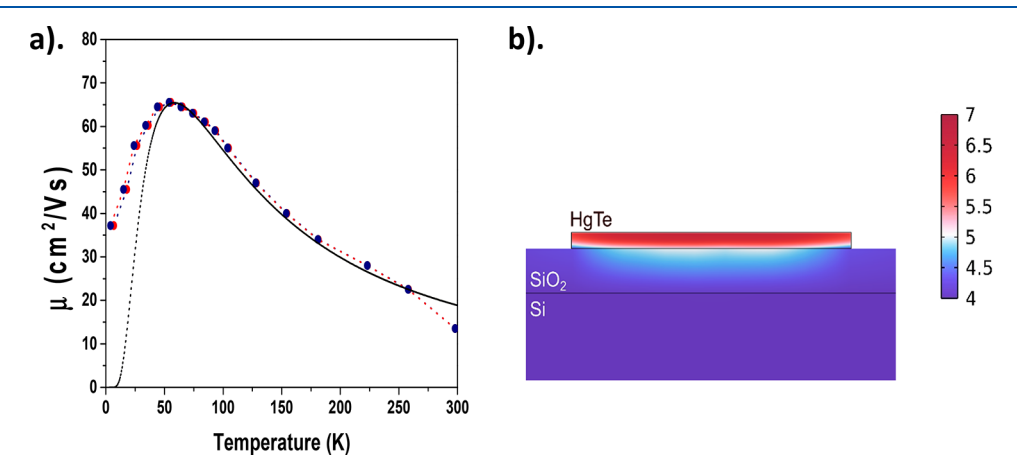


Figure 5. (a) Measured differential mobility with the cryostat (blue) and simulated (red) temperature after considering Joule heating. The dash-dotted line is the Marcus hopping model fitted to the higher temperature and low bias mobility. (b) Cross section of the device with dissipating thermal power at high biases. The sink is set at the bottom of the silicon wafer at T = 4 K.

pulse across 2 μ m devices at 4 K. There are a few "burned" paths in the device, with the width of such paths on the order of 100 nm, a width that is similar to the localization length. In these destructive experiments, we also applied a steady 10 V bias and then observed a stepwise decrease in the conductance, as if discrete paths were burned out one after the other. One possibility is that it is the paths of higher conductance which are the first to overheat due to the large amount of power flowing through and that this leaves them as patterns of destruction visible by SEM.

Besides basic interest in transport in CQD films, an additional motivation to explore higher mobility CQD films is the conjectured reduction of 1/f noise. 31 1/f noise is briefly discussed in the Supporting Information and shown in Figure S2d. Figure S3 semiquantitatively confirms the conjecture for the high mobility films studied here.

Joule Heating during Measurement. When discussing nonlinear electrical properties at a low temperature, it is important to evaluate the possibility of Joule heating. Here, the observation of nonzero mobility as the sample approaches 0 K could be the consequence of a rising sample temperature rather

than the field-driven effect discussed above. To address this point, COMSOL simulations were conducted to estimate Joule heating in the device featuring a 2 μ m long channel.

The simulated system consists of a 1 cm \times 1 cm substrate with a 400 μm thick silicon layer and a 300 nm thick SiO₂ layer. On top of the oxide, the HgTe CQD channel is defined as a 100 μm imes 2 μm layer with 100 nm thickness. The electrical power P dissipated as heat in the device was calculated using $P = V^2/R$ with values of the resistance R extracted from the experimental I-V curves and V = 0.4 V as the maximum bias applied during voltage sweeps. The influence of the electrodes on heat dissipation is neglected, and all the dissipated electrical power is distributed homogeneously over the volume of the HgTe CQD channel. To mimic the situation of a sample in contact with a cryostat, the back surface of the silicon substrate is defined as a thermostat with a set temperature. We assumed ideal thermal contact at the interface between the QDs film and the substrate, while the boundaries of the system were defined as perfect thermal insulators. Temperature-dependent thermal conductivities were taken from the literature for the Si layer

and the SiO₂ layer, and they are given in Figure S4.^{32,33} In the absence of data for the thermal conductivity of the HgTe CQD film, we purposely underestimated it to overestimate the temperature rise. We used a thermal conductivity of 1/20th of the thermal conductivity of SiO₂ (Figure S4). This corresponds to less than 0.015 W/(m K) below 100 K and less than 0.005 W/(m K) below 10 K, while reported room temperature thermal conductivity for nanocrystal solids is $\sim 0.1-0.4 \text{ W/(m K)}.^{34}$ The average temperature in the film is calculated in the stationary regime, and no further investigation has been made to know if thermal equilibrium is reached during the voltage sweeps performed in the experiments.

Figure 5b shows the calculated temperature across the cross section of the system for values of the dissipated electrical power and cryostat temperature corresponding to the mobility measurement at 4 K. We observe that the calculated temperature in the CQD film is a few kelvin higher than the temperature of the cryostat. Running the simulation with parameters corresponding to each data point of Figure 1b, we obtain a new set of adjusted temperatures for the HgTe CQDs. Figure 5a presents the mobility measurements performed on the 2 μ m device with adjusted temperatures obtained from the simulations along with the experimental data reproduced from Figure 1b. The largest difference from the experimental curve occurs at low temperature and is limited to a few kelvin, which slightly alters the shape of the curve but does not change the results of the experiments. Additional simulations were also made by adding a thick SiO₂ layer on the back of the substrate, resulting in an increase of the temperature by only 1000th of a kelvin. The simulation therefore supports field effect rather than Joule heating as the main cause of the high mobility at high bias and low temperatures.

IV. CONCLUSION

This work explored the state-resolved electronic transport of a disordered film of HgTe quantum dots with one partially occupied state per dot. Using the same hybrid ligand exchange as previously reported, but with slightly larger dots and narrower size distribution, accompanied by a narrower intraband absorption, the 1S_e state mobility, at a filling ~0.5 electrons per dot, was 8 times larger than in prior work, reaching 65 cm²/(V s) with the narrowest channel length devices of 2 μ m at 65 K.

At temperatures above 70 K, the transport was ohmic within the bias range studied, and the mobility was band-like, increasing with decreasing temperature. Yet, data were quantitatively fitted to the Marcus hopping model. The higher mobility than in prior work is consistent with slightly lower values of the energy disorder, slightly larger dot sizes, and a slightly larger coupling. The mobility achieved is much lower than the 3000 $\text{cm}^2/(\text{V s})$ estimated for the Mott–Ioffe–Regel limit, and the average interdot conductance is also much smaller than the quantum conductance, all supporting hopping

Data at lower temperatures strain the applicability of the hopping transport. At 65 K, the average hopping time is evaluated to be around 1 ps, which is getting close to the estimated coherence time of the 1S_e state of 0.7 ps. At lower temperatures below 70 K, and at high bias, the film resistance remains constant on the way to 0 K, mimicking metallic transport, but this is fully explained using the variable range hopping model and field-driven transport. The low bias and high bias data provided the VRH parameters T^* and E^* . These

gave two independent but consistent determinations of the localization lengths of 70 nm for the 10 μ m channel and increasing to 100 nm for the 2 μ m channel. These lengths are 2-3 times longer than in previous work and suggest the possibility of small regions of delocalized transport in the films, and this may explain why a higher mobility is obtained for the smaller electrode channel lengths.

This work shows that making larger HgTe CQD with a narrower size dispersion is a route toward higher mobility, while keeping a rather small coupling strength, and it should motivate further effort in this direction, toward more delocalized state-resolved transport.

ASSOCIATED CONTENT

Supporting Information

The Supporting Information is available free of charge at https://pubs.acs.org/doi/10.1021/acs.jpcc.3c07908.

SEM image of dots on the FET chip and variation of the electrode gap; SEM images of films on the FET chip and 1/f current noise; Hooge constant as a function of interdot conductance; thermal conductivity used for the thermal simulation (PDF)

AUTHOR INFORMATION

Corresponding Author

Philippe Guyot-Sionnest – The James Franck Institute, The University of Chicago, Chicago, Illinois 60637, United States; o orcid.org/0000-0003-0178-6255; Email: pgs@ uchicago.edu

Authors

Haozhi Zhang - The James Franck Institute, The University of Chicago, Chicago, Illinois 60637, United States; orcid.org/0000-0001-6854-2162

John C. Peterson – The James Franck Institute, The University of Chicago, Chicago, Illinois 60637, United States; orcid.org/0000-0002-0509-6959

Augustin Caillas – The James Franck Institute, The University of Chicago, Chicago, Illinois 60637, United States; orcid.org/0009-0007-9075-9449

Complete contact information is available at: https://pubs.acs.org/10.1021/acs.jpcc.3c07908

The authors declare no competing financial interest.

ACKNOWLEDGMENTS

This work was supported by ONR Grant N00014-22-1-2027. This work also made use of the shared facilities at the University of Chicago Materials Research Science and Engineering Center, supported by National Science Foundation under Award DMR-2011854, the Pritzker Nanofabrication Facility part of the Pritzker School of Molecular Engineering at the University of Chicago, which receives support from Soft and Hybrid Nanotechnology Experimental (SHyNE) Resource (NSF 21 ECCS-2025633), a node of the National Science Foundation's National Nanotechnology Coordinated Infrastructure, and the University of Chicago's Research Computing Center.

REFERENCES

- (1) García de Arquer, F. P.; Talapin, D. V.; Klimov, V. I.; Arakawa, Y.; Bayer, M.; Sargent, E. H. Semiconductor Quantum Dots: Technological Progress and Future Challenges. *Science* **2021**, DOI: 10.1126/science.aaz8541.
- (2) Lee, J.-S.; Kovalenko, M. V.; Huang, J.; Chung, D. S.; Talapin, D. V. Band-like Transport, High Electron Mobility and High Photoconductivity in All-Inorganic Nanocrystal Arrays. *Nat. Nanotechnol.* **2011**, *6* (6), 348–352.
- (3) Kagan, C. R.; Murray, C. B. Charge Transport in Strongly Coupled Quantum Dot Solids. *Nat. Nanotechnol.* **2015**, *10* (12), 1013–1026.
- (4) Choi, J.-H.; Fafarman, A. T.; Oh, S. J.; Ko, D.-K.; Kim, D. K.; Diroll, B. T.; Muramoto, S.; Gillen, J. G.; Murray, C. B.; Kagan, C. R. Bandlike Transport in Strongly Coupled and Doped Quantum Dot Solids: A Route to High-Performance Thin-Film Electronics. *Nano Lett.* **2012**, *12* (5), 2631–2638.
- (5) Balazs, D. M.; Matysiak, B. M.; Momand, J.; Shulga, A. G.; Ibáñez, M.; Kovalenko, M. V.; Kooi, B. J.; Loi, M. A. Electron Mobility of 24 cm²/Vs in PbSe Colloidal-Quantum-Dot Superlattices. *Adv. Mater.* **2018**, *30* (38), No. 1802265.
- (6) Pinna, J.; Mehrabi Koushki, R.; Gavhane, D. S.; Ahmadi, M.; Mutalik, S.; Zohaib, M.; Protesescu, L.; Kooi, B. J.; Portale, G.; Loi, M. A. Approaching Bulk Mobility in PbSe Colloidal Quantum Dots 3D Superlattices. *Adv. Mater.* **2023**, *35* (8), No. 2207364.
- (7) Collier, C. P.; Saykally, R. J.; Shiang, J. J.; Henrichs, S. E.; Heath, J. R. Reversible Tuning of Silver Quantum Dot Monolayers Through the Metal-Insulator Transition. *Science* **1997**, 277 (5334), 1978–1981.
- (8) Zabet-Khosousi, A.; Trudeau, P.-E.; Suganuma, Y.; Dhirani, A.-A.; Statt, B. Metal to Insulator Transition in Films of Molecularly Linked Gold Nanoparticles. *Phys. Rev. Lett.* **2006**, *96* (15), No. 156403.
- (9) Coropceanu, I.; Janke, E. M.; Portner, J.; Haubold, D.; Nguyen, T. D.; Das, A.; Tanner, C. P. N.; Utterback, J. K.; Teitelbaum, S. W.; Hudson, M. H.; Sarma, N. A.; Hinkle, A. M.; Tassone, C. J.; Eychmuller, A.; Limmer, D. T.; Olvera de la Cruz, M.; Ginsberg, N. S.; Talapin, D. V. Self-Assembly of Nanocrystals into Strongly Electronically Coupled All-Inorganic Supercrystals. *Science* 2022, 375 (6587), 1422–1426.
- (10) Guyot-Sionnest, P. Electrical Transport in Colloidal Quantum Dot Films. *J. Phys. Chem. Lett.* **2012**, 3 (9), 1169–1175.
- (11) Fu, H.; Reich, K. V.; Shklovskii, B. I. Hopping Conductivity and Insulator-Metal Transition in Films of Touching Semiconductor Nanocrystals. *Phys. Rev. B* **2016**, *93* (12), No. 125430.
- (12) Chen, T.; Reich, K. V.; Kramer, N. J.; Fu, H.; Kortshagen, U. R.; Shklovskii, B. I. Metal—Insulator Transition in Films of Doped Semiconductor Nanocrystals. *Nat. Mater.* **2016**, *15* (3), 299–303.
- (13) Greenberg, B. L.; Robinson, Z. L.; Reich, K. V.; Gorynski, C.; Voigt, B. N.; Francis, L. F.; Shklovskii, B. I.; Aydil, E. S.; Kortshagen, U. R. ZnO Nanocrystal Networks Near the Insulator—Metal Transition: Tuning Contact Radius and Electron Density with Intense Pulsed Light. *Nano Lett.* **2017**, *17* (8), 4634–4642.
- (14) Greenberg, B. L.; Robinson, Z. L.; Ayino, Y.; Held, J. T.; Peterson, T. A.; Mkhoyan, K. A.; Pribiag, V. S.; Aydil, E. S.; Kortshagen, U. R. Metal-Insulator Transition in a Semiconductor Nanocrystal Network. *Sci. Adv.* **2019**, *5* (8), No. eaaw1462.
- (15) Septianto, R. D.; Miranti, R.; Kikitsu, T.; Hikima, T.; Hashizume, D.; Matsushita, N.; Iwasa, Y.; Bisri, S. Z. Enabling Metallic Behaviour in Two-Dimensional Superlattice of Semiconductor Colloidal Quantum Dots. *Nat. Commun.* **2023**, *14* (1), 2670.
- (16) Lan, X.; Chen, M.; Hudson, M. H.; Kamysbayev, V.; Wang, Y.; Guyot-Sionnest, P.; Talapin, D. V. Quantum Dot Solids Showing State-Resolved Band-like Transport. *Nat. Mater.* **2020**, *19* (3), 323–329.
- (17) Chen, M.; Lan, X.; Tang, X.; Wang, Y.; Hudson, M. H.; Talapin, D. V.; Guyot-Sionnest, P. High Carrier Mobility in HgTe

- Quantum Dot Solids Improves Mid-IR Photodetectors. ACS Photonics **2019**, 6 (9), 2358–2365.
- (18) Chen, M.; Guyot-Sionnest, P. Reversible Electrochemistry of Mercury Chalcogenide Colloidal Quantum Dot Films. *ACS Nano* **2017**, *11* (4), 4165–4173.
- (19) Tian, Y.; Luo, H.; Chen, M.; Li, C.; Kershaw, S. V.; Zhang, R.; Rogach, A. L. Mercury Chalcogenide Colloidal Quantum Dots for Infrared Photodetection: From Synthesis to Device Applications. *Nanoscale* **2023**, *15* (14), 6476–6504.
- (20) Fratini, S.; Mayou, D.; Ciuchi, S. The transient localization scenario for charge transport in crystalline organic materials. *Adv. Funct. Mater.* **2016**, *26* (14), 2292–2315.
- (21) Hudson, M. H.; Chen, M.; Kamysbayev, V.; Janke, E. M.; Lan, X. Z.; Allan, G.; Delerue, C.; Lee, B.; Guyot-Sionnest, P.; Talapin, D. V. Conduction band fine structure in colloidal HgTe quantum dots. *ACS Nano* **2018**, *12*, 9397–9404.
- (22) Zhang, H.; Peterson, J. C.; Guyot-Sionnest, P. Intraband Transition of HgTe Nanocrystals for Long-Wave Infrared Detection at 12 μ m. ACS Nano 2023, 17 (8), 7530–7538.
- (23) Shen, G.; Chen, M.; Guyot-Sionnest, P. Synthesis of Nonaggregating HgTe Colloidal Quantum Dots and the Emergence of Air-Stable n-Doping. J. Phys. Chem. Lett. 2017, 8 (10), 2224–2228.
- (24) Zhang, H.; Guyot-Sionnest, P. Shape-Controlled HgTe Colloidal Quantum Dots and Reduced Spin-Orbit Splitting in the Tetrahedral Shape. *J. Phys. Chem. Lett.* **2020**, *11* (16), 6860–6866.
- (25) Yang, J.; Hu, H.; Lv, Y.; Yuan, M.; Wang, B.; He, Z.; Chen, S.; Wang, Y.; Hu, Z.; Yu, M.; Zhang, X.; He, J.; Zhang, J.; Liu, H.; Hsu, H.-Y.; Tang, J.; Song, H.; Lan, X. Ligand-Engineered HgTe Colloidal Quantum Dot Solids for Infrared Photodetectors. *Nano Lett.* **2022**, 22 (8), 3465–3472.
- (26) Chu, I.-H.; Radulaski, M.; Vukmirovic, N.; Cheng, H.-P.; Wang, L.-W. Charge Transport in a Quantum Dot Supercrystal. *J. Phys. Chem. C* 2011, 115 (43), 21409–21415.
- (27) Prodanović, N.; Vukmirović, N.; Ikonić, Z.; Harrison, P.; Indjin, D. Importance of Polaronic Effects for Charge Transport in CdSe Quantum Dot Solids. *J. Phys. Chem. Lett.* **2014**, *5* (8), 1335–1340.
- (28) Shklovskii, B. I.; Efros, A. L. Variable-Range Hopping Conduction. In *Electronic Properties of Doped Semiconductors*; Shklovskii, B. I., Efros, A. L., Eds.; Springer Series in Solid-State Sciences; Springer: Berlin, 1984; pp 202–227.
- (29) Skinner, B.; Chen, T.; Shklovskii, B. I. Theory of Hopping Conduction in Arrays of Doped Semiconductor Nanocrystals. *Phys. Rev. B* **2012**, *85* (20), No. 205316.
- (30) Yu, D.; Wang, C.; Wehrenberg, B. L.; Guyot-Sionnest, P. Variable Range Hopping Conduction in Semiconductor Nanocrystal Solids. *Phys. Rev. Lett.* **2004**, 92 (21), No. 216802.
- (31) Liu, H.; Lhuillier, E.; Guyot-Sionnest, P. 1/f noise in semiconductor and metal nanocrystal solids. *J. Appl. Phys.* **2014** *115* (15).
- (32) Glassbrenner, C. J.; Slack, G. L. Thermal Conductivity of Silicon and Germanium from 3K to the Melting Point. *Phys. Rev.* **1964**, 134, A1058.
- (33) Pohl, R. O.; Liu, X.; Thompson, E. J. Low-temperature thermal conductivity and acoustic attenuation in amorphous solids. *Rev. Mod. Phys.* **2002**, *74*, 991.
- (34) Wang, Z.; Christodoulides, A. D.; Dai, L.; Zhou, Y.; Dai, R.; Xu, Y.; Nian, Q.; Wang, J.; Malen, J. A.; Wang, R. Y. Nanocrystal Ordering Enhances Thermal Transport and Mechanics in Single-Domain Colloidal Nanocrystal Superlattices. *Nano Lett.* **2022**, *22*, 4669–4676.